



Operando Raman Micro-Spectroscopy of Polymer Electrolyte Fuel Cells

Ian Kendrick,^a Jennifer Fore,^a Jonathan Doan,^a Neili Loupe,^{a,*} Andy Vong,^a
Nicholas Dimakis,^b Max Diem,^a and Eugene S. Smotkin^{a,**,z}

^aDepartment of Chemistry and Chemical Biology, Northeastern University, Boston, Massachusetts 02115, USA

^bDepartment of Physics, University of Texas Rio Grande Valley, Edinburg, Texas 78539, USA

Operando Raman micro-spectroscopy of the membrane electrode assembly (MEA) of a fully operating hydrogen/oxygen Nafion electrolyte fuel cell is described. Coarse depth profiling of the fuel cell system enabled appropriate positioning of the micro-spectroscopy laser focal point for MEA catalytic layer spectroscopy. An increase in the ionomer state-of-hydration, from oxygen reduction at the cathode, transitions ion exchange sites from the sulfonic acid to the dissociated sulfonate form. Visualization of density functional theory calculated normal mode eigenvector animations enabled assignments of Nafion side-chain vibrational bands in terms of the exchange site local symmetry: C₁ and C_{3v} modes correlate to the sulfonic acid and sulfonate forms respectively. The gradual transition of the MEA spectra from C₁ to C_{3v} modes, from the fuel cell open circuit voltage to the short circuit current respectively, demonstrate the utility of vibrational group mode assignments in terms of exchange site local symmetry.

© The Author(s) 2016. Published by ECS. This is an open access article distributed under the terms of the Creative Commons Attribution 4.0 License (CC BY, <http://creativecommons.org/licenses/by/4.0/>), which permits unrestricted reuse of the work in any medium, provided the original work is properly cited. [DOI: 10.1149/2.0211604jes] All rights reserved.

Manuscript submitted October 15, 2015; revised manuscript received December 26, 2015. Published January 16, 2016. This was Paper 1537 presented at the Seattle, Washington, Meeting of the Society, May 6–10, 2012. *This paper is part of the JES Focus Issue Honoring Allen J. Bard.*

Because the active state of a fuel cell catalyst exists only during catalysis,¹ the relevant conditions under which electrocatalysts should be characterized are with potential control and incorporated into a membrane electrode assembly (MEA) exposed to flowing reactant streams. In situ methods, applied to practical devices, are termed “operando”. Although practiced for decades, “operando” first appeared in the literature in 2002.²

Figure 1 schematizes a single cell of a fuel cell housing a 5-layer MEA. MEA catalytic layers are made by deposition of catalyst inks upon either the carbon gas diffusion layers or directly onto the membrane.³ Catalyst inks are carbon supported catalysts dispersed in an alcoholic dispersion of solubilized ionomer (e.g., Nafion). Teflon dispersion is included in cathode inks to lower the surface free energy and prevent water, formed during oxygen reduction, from condensing. Unsupported metal blacks are used for direct methanol fuel cells. Methods for MEA preparation have been reviewed.⁴

Our first approach to realistic evaluation of catalysts was our deposition of direct methanol fuel cell catalyst inks onto glassy carbon rotating disk electrodes.^{5,6} Operando infrared (IR) spectroscopy of fuel cells was introduced by Fan et al. using a CaF₂ windowed fuel cell installed within a Harrick diffuse reflectance sample compartment.⁷ This was followed by operando X-ray absorption spectroscopy (XAS) of hydrogen air fuel cells initiated by Viswanathan et al.^{8,9} and liquid feed direct methanol fuel cells by Stoupin et al.¹⁰ Details of the operando XAS cell were published⁹ and similar versions of this cell were used by Principe¹¹ and Russell.¹² Operando XAS of fuel cells is now widely practiced.^{13–17}

A hydrated membrane is essential for fuel cell operation. Operando IR spectroscopy^{7,18–27} requires stringent control of reactant stream humidification, flow rate, and cell temperature to prevent condensed water from overwhelming the IR spectra. Raman micro-spectroscopy, which is tolerant of condensed water, is complementary to FTIR.

Operando Raman spectroscopy of solid oxide fuel cells has been reported.^{28–30} Although there are reports of operando PEM fuel cell water management/transport studies,^{31–36} no potential-dependent data was provided. This H₂/air fuel cell spectroscopy uses density functional theory (DFT) calculated normal mode analysis of the Nafion side chain and perfluorinated small molecules to correlate variation of

Nafion vibrational group modes with fuel cell cathode potentials. Water formation at the cathode directly impacts the Nafion ion exchange site local symmetry. This provides a basis for proper assignment of Nafion vibrational group modes.

Additionally, preliminary results on fuel cell assembly depth profiling show that the Raman laser can penetrate the MEA catalytic layer. This enabled, for the first time, the profiling of a *device structure* from the center of an MEA, through the catalytic layer, and up to and including the flow field region. This low resolution device profiling enables proper positioning of the laser focal point for study of the catalytic layer.

Experimental

Molecular modeling calculations.—Unrestricted DFT³⁷ with the X3LYP³⁸ functional was used for geometry optimizations and normal mode frequency calculations of (a) hydrated Nafion-[H], (b) dehydrated Nafion-[H], (c) 2-trifluoromethoxy-perfluoroethane-2-sulfonate (TPS[−]), (d) 2-trifluoromethoxy-perfluoroethane-2-sulfonic acid (TPSH), (e) triflate, (f) triflic acid, and (g) di(trifluoromethyl)ether (DTFME) (Fig. 2).

The X3LYP is an extension to the B3LYP³⁹ functional providing more accurate heats of formation. Jaguar 8.7 (Schrodinger Inc., Portland, OR) was used with the all-electron 6–311G**++ Pople triple- ζ basis set (“***” and “++” denote polarization³⁷ and diffuse⁴⁰ basis set functions, respectively). Output files were converted to vibrational mode animations using the Maestro graphical user interface (Schrodinger Inc., New York, NY). Calculations were carried out on the high performance computing cluster at the University of Texas Rio Grande Valley with 72 nodes of Dual 2.67 Ghz processors; each node with 48 GB RAM and 250 GB disk. DFT calculated normal mode peaks are denoted by superscript (*) (e.g., 983* cm^{−1}). Only normal modes with normalized intensity above 1% of the largest peak were selected for Maestro animation viewing.

Non-PGM catalyst preparation.—Non-platinum group (non-PGM) catalysts were prepared and provided by Barton, et al.⁴¹ Briefly, in their preparative method, Ketjen black 600JD (Akzo Nobel, Amsterdam, Netherlands), iron acetate (0.75 wt% Fe) (Alfa Aesar, Ward Hill, MA) and melamine (6.3 wt% N) (Alfa Aesar) were heat treated at 800°C. These catalysts were used as received.

*Electrochemical Society Student Member.

**Electrochemical Society Member.

^zE-mail: e.smotkin@neu.edu

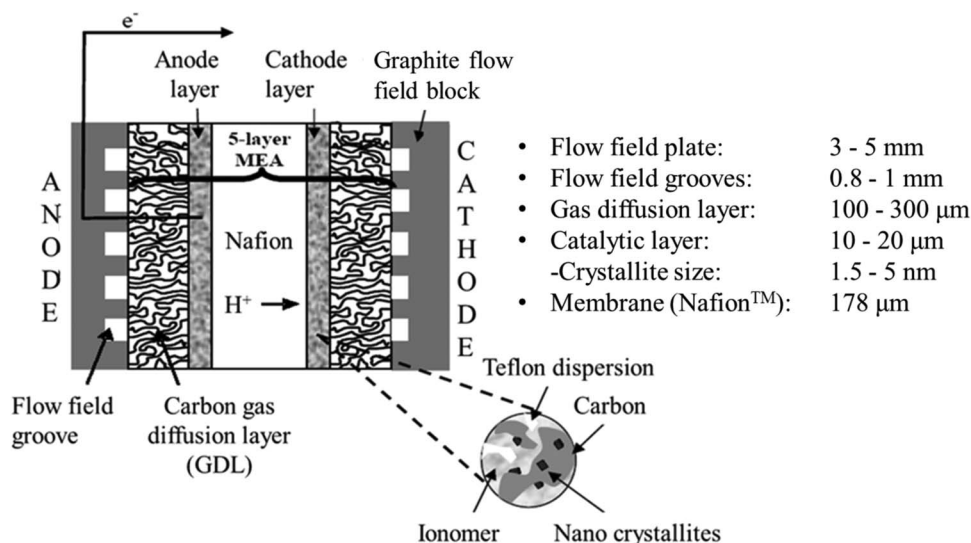


Figure 1. Single cell fuel cell with Nafion 117 5-layer membrane electrode assembly.

MEA Preparation.—Nafion 117 (Wilmington, DE) was pretreated by immersing sheets in boiling 8 M nitric acid followed by two hours in boiling Nanopure™ water. Catalyst inks were prepared by diluting the catalyst in 5 wt% Nafion ionomer solution (Sigma Aldrich, Milwaukee, WI), water, and isopropyl alcohol (Sigma Aldrich). 4 mg/cm² Pt black (Johnson Matthey, London, UK) and 1.6 mg/cm² non-PGM catalyst were used as the anode and cathode catalysts, respectively. Catalyst inks were applied to a 5 cm² area of a sheet of Nafion 117 (E. I. DuPont) immobilized on a heated vacuum table (NuVant Systems, Inc., Crown Point, IN). Toray carbon paper (200 μm) was used for the gas diffusion layers. MEAs were initially conditioned by cycling the potential from 200–800 mV in the operando Raman cell operating at 50°C with humidified H₂ (50 sccm) and O₂ (200 sccm) flowing over the anode and cathode, respectively.

Cell design.—The operando Raman fuel cell design (Fig. 3) is a modification of the operando IR-XAS cell described by Lewis et al.²¹ Briefly, the upper flow field connects to the working electrode and contains an aperture that accommodates a GE 124 fused quartz window (General Electric). The lower flow field connects to the counter/reference electrode to which humidified hydrogen is delivered. The counter and reference electrodes of the EZstat Pro po-

tentiostat/ galvanostat (NuVant Systems Inc., Crown Point, IN 46307) are shorted together and connected to the counter/reference electrode. The cell is connected to a gas manifold that delivers the reactant feeds to the anode and cathode graphite flow fields. The cell is equipped with heater elements and a thermistor for temperature control. A DB9 connector interfaces the EZstat Pro to the operando cell. The cell is positioned at the working distance of the microscope objective (Fig. 3).

Operando Raman spectroscopy.—All operando Raman spectra were acquired using a WITec Inc. (Ulm, Germany) Confocal Raman Microscope (CRM 200). A 488 nm (23 mW) solid state laser (WITec Inc.) was used as the excitation source, which was coupled into a Zeiss (Thornwood, NY) microscope *via* a 50 μm wavelength-specific single-mode optical fiber. The incident laser beam was focused onto the sample using a Nikon (Tokyo, Japan) Fluor (10x/0.25, WD: 7.00 mm) objective with a z resolution of 23 μm and confocal volume of 33 μm³. The Raman backscattered radiation was focused through a holographic notch filter, onto a 50 μm multimode optical fiber, and into a 300 mm focal length monochromator (600/mm grating, blazed at 500 nm). The Raman spectrum was detected *via* a back-illuminated, deep-depletion CCD camera (1024×128 pixels) operating at –82°C. Single Raman spectra were acquired for 30s, except that spectra of the Fe based catalyst under O₂ conditions were obtained with a 30 second acquisition time and a hardware accumulation of 2s. Confocal microscope depth profiling was performed with a step size of 50 μm. Because the confocal volume of the 10x objective is 33 μm³, spectra are correlated to overlapping layers of the assembly structure as shown in the Results section.

Prior to obtaining spectra, the cell potential was cycled from 0 to 1200 mV at 50°C with humidified H₂ (50 sccm) and N₂ (200 sccm) fed to the counter/reference and working electrodes, respectively. The working electrode reactant feed was then switched to humidified O₂ (200 sccm). Raman spectra were obtained between 1100 mV and 0 mV and collected in decreasing 100 mV increments. The fuel cell anode was used as the reference electrode by shorting the counter and reference electrodes of the potentiostat (EZstat Pro, NuVant Systems, Crown Point, IN 46307) as described by Gurau et al.⁴²

Results

Location of optimal focal point for study of catalytic layer.—Our interest in cathode catalytic layer processes within the operando cell required determination of the optimal position of the Raman microscope laser beam focal point. Figure 4 shows a cross sectional

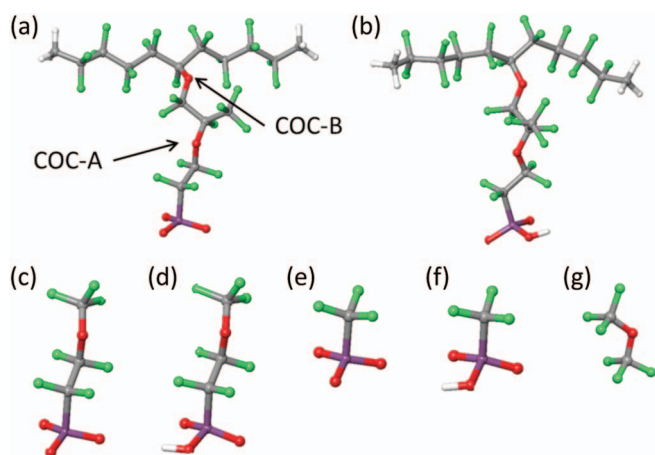


Figure 2. Model structures for DFT normal mode analysis. (a) hydrated Nafion-[H], (b) dehydrated Nafion-[H], (c) TPS[−], (d) TPSH, (e) triflate, (f) triflic acid, and (g) DTFME.

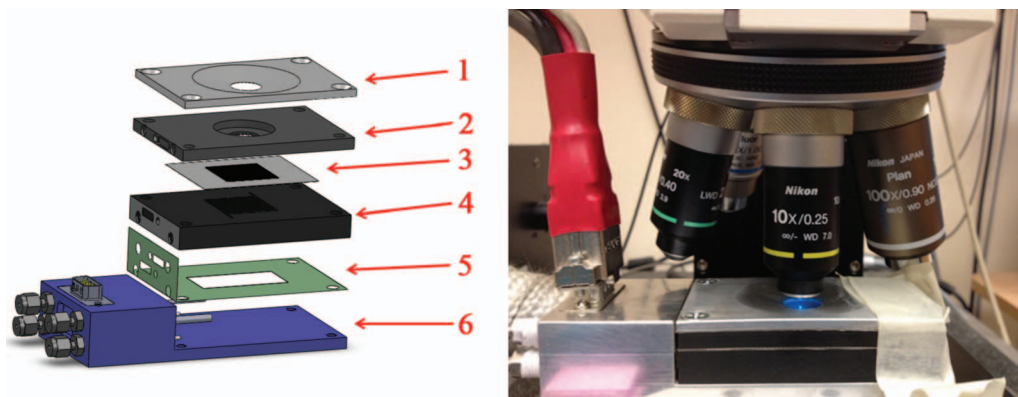


Figure 3. Left: Exploded view of the operando Raman cell. (1) Top plate, (2) Upper flow field, (3) Membrane electrode assembly, (4) Lower flow field, (5) Assembly gasket, and (6) Assembly stage. Right: Operando Raman cell in position for confocal Raman microscopy.

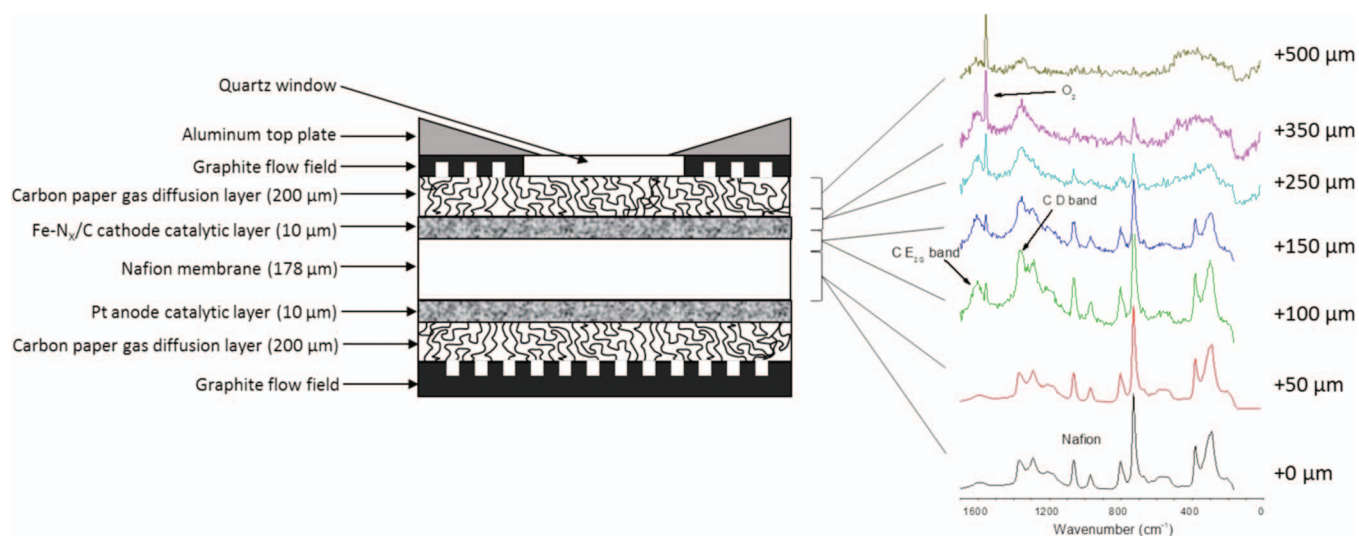


Figure 4. Left: Schematic of MEA installed in the operando spectroscopy fuel cell. Right: Confocal Raman microscope depth profiling spectra of Fe-N_x/C cathode with humidified O₂ flow.

schematic of the MEA loaded into the operando cell (Fig. 4, left). The microscope focal point was varied along the z-axis until the Nafion spectrum attained a maximum intensity (black spectrum). This is the “reference” position for additional spectra obtained as the focal point was sequentially lifted above the reference (Fig. 4, right). This is “device” depth profiling over four complex regions (membrane, catalytic layer, gas diffusion layer and graphite flow field region). The Nafion membrane is a ~ 178 μm condensed phase that, within the torques applied to fuel cell (35 in-lbs / 8 bolts: 4 in. on edge flow field blocks), is incompressible. The nevertheless complex optics for membrane(s) layers is discussed by Peng et al.³¹ The catalytic layer is a ~ 10 μm porous composite layer with optical characteristics that substantially vary with electrode potential.²² The gas diffusion layer is a ~ 200 μm porous carbon paper that is homogenous over a length scale of microns. The final layer is a dense graphite layer with millimeter flow field grooves and an aperture to fit a quartz window.

The focal point position (or depth) cannot be directly correlated to a position within the fuel cell assembly. The z resolution of 23 μm and confocal volume of 33 μm^3 , compounded by the physical characteristics of the different layers (e.g., thickness, diffraction, scattering, etc.) add to Raman signal distortion.^{31,34} Each focal point location (Fig. 4, Right) yields signal over a bracketed region of the fuel cell assembly. Fortunately, bracketed regions can be calibrated by knowledge of the nominal compositions of the device regions (e.g. pure polymer regions, carbon support, gaseous dioxygen, etc.). Gaseous dioxygen is not observable within the incompressible membrane. At a focal point

of +150 μm (from the reference position), a dioxygen peak emerges at 1556 cm^{-1} . Gaseous oxygen resides in the porous cathode layer, the gas diffusion layer and in the flow field. The oxygen band is not observed within the Nafion membrane region with detection limits of 1000 ppm).^{43–45,c}

Peaks related to the carbon support in the catalytic layer start to emerge at +100 μm with no attenuation of the Nafion peaks. The two prominent features of the graphite are the E_{2g} vibration mode at 1600 cm^{-1} and disorder peak (D peak) at 1360 cm^{-1} .⁴⁶ The D peak, which arises from an A_{1g} breathing mode, is observed at the edges of graphene planes on clusters smaller than 200 Å.⁴⁶ The catalytic layer is rendered ionically conductive by Nafion ionomer originating from the catalyst ink.³

Our objectives required that we select the highest focal point available that exhibited dioxygen peaks simultaneously with Nafion peaks. Based on Figure 4 (Right), we selected + 350 μm above the reference.

Potential-dependent Raman bands.—The polarization curve, obtained with the focal point set at +350 μm from the reference, (Fig. 5) shows a current onset at 750 mV (a striking 20-fold improvement over carbon with no iron-based catalyst).⁴⁷ At cathode potentials positive of 800 mV (Fig. 6) there is no current and thus no oxygen reduction reaction (ORR). Figure 6 compares potential-dependent Raman spectra

^cThe expected solubility of oxygen within the membrane (50°C and ~ 30 water molecules/exchange site) is 8.9 ppm.

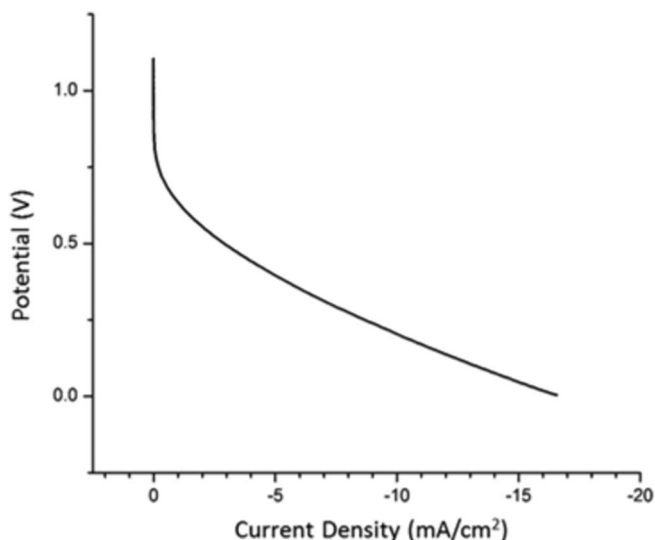


Figure 5. Polarization curve obtained in the operando spectroscopy fuel cell. Pt anode (humidified H_2); Fe-N_x/C cathode (humidified O_2).

(left) with transmission IR spectra of fully dehydrated (blue), partially hydrated (purple) and fully hydrated (red) Nafion. The Raman spectra in the ORR inactive region (positive of 800 mV) exhibit a band at 910 cm^{-1} that is also observed in the spectrum of dehydrated Nafion (blue)). This mode has been established to be dominated by motions of the Nafion exchange site in the sulfonic acid form that has no local symmetry (C_1).^{22,48–50}

At potentials negative of 700 mV, Raman bands at 1066 cm^{-1} and 969 cm^{-1} emerge. These bands, also observed in the hydrated Nafion (red) IR spectrum, are the $C_{3V, HF}$ and $C_{3V, LF}$ group modes respectively. These group modes are consequent of a dissociated Nafion exchange site (sulfonate form) with C_{3V} local symmetry.^{22,48,51–55}

C_1 normal mode eigenvector animation snapshots.—The dehydrated Nafion spectrum (blue) features bands at 1414 cm^{-1} and 910 cm^{-1} . These are group modes that have motional participation of the exchange group in the sulfonic acid form (C_1 local symmetry). Eigenvector animation extrema screenshots (Fig. 7, top panels) provide details of the vibrational motions with the dominant motions within solid circles and secondary contributions within dotted circles. These high and low frequency bands ($C_{1, HF}$ and $C_{1, LF}$, respectively) correspond to group modes that involve the side-chain functional group contributions (e.g., COC-A, $-\text{CF}_3$, exchange site, etc.). The $C_{1, HF}$ and $C_{1, LF}$ group modes are both dominated by sulfonic acid stretching (asymmetric and symmetric, respectively) with secondary contributions from COC-A stretching (asymmetric and symmetric, respectively). The lower panels show eigenvector extrema snapshots of molecules that make up the pure modes contributing to the C_1 group modes, along with associated calculated normal mode frequencies. The mirrored similarities of dehydrated Nafion group modes and side chain pure modes is evident (Fig. 7). Comparison of the pure modes (bottom panels) with the calculated normal modes (top panels) correctly show that the pure mode frequencies contributing to the $C_{1, LF}$ are on average substantially higher than the pure modes contributing to the $C_{1, HF}$, in support of the assignments. The relationships between the pure modes and the calculated normal modes (actually group modes) are more explicit by visualization of the video animations (Supplemental Material (Figs. S6, 8, 11–12, 14–17). A similar analysis for C_{3V} peaks that emerge as the fuel cell potential is decreased follows. All of the assignments are summarized in Table I.

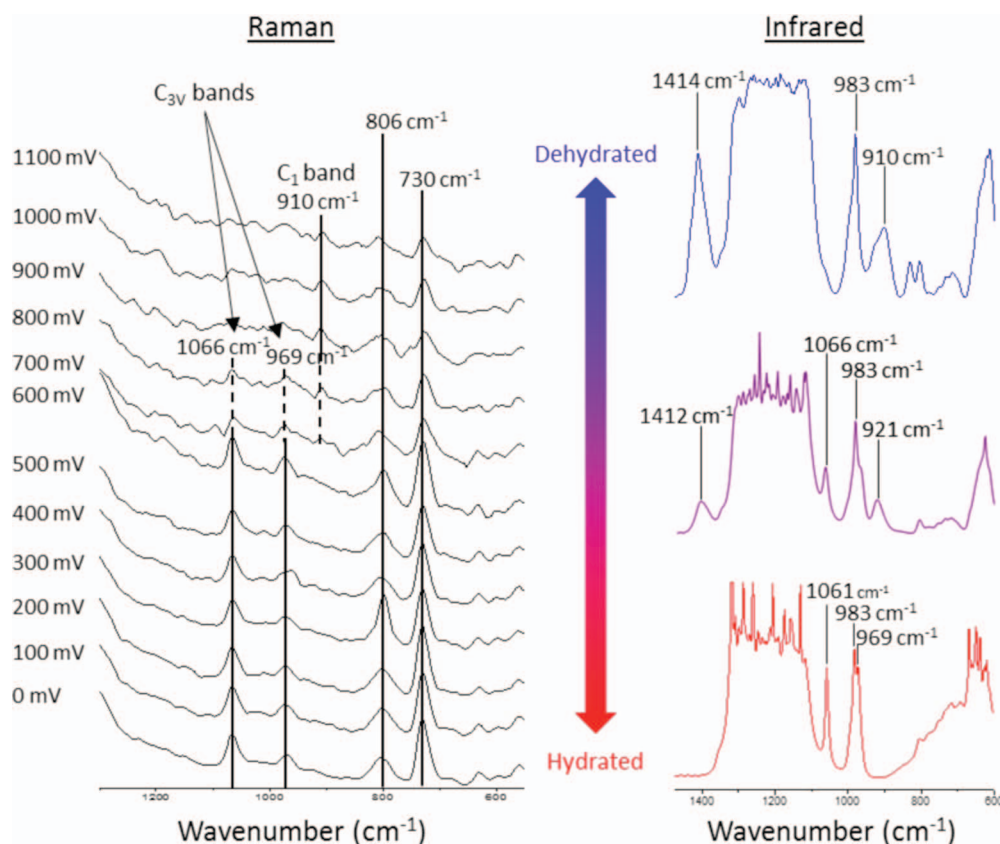


Figure 6. Left: Potential dependent Raman spectra of Fe-N_x/C cathode catalyst with O_2 at cathode; H_2 at the anode. Right: Transmission spectra of Nafion 212. Fully dehydrated (top), partially dehydrated (middle) and fully hydrated (bottom). Group theory labels refer to exchange site local symmetry.

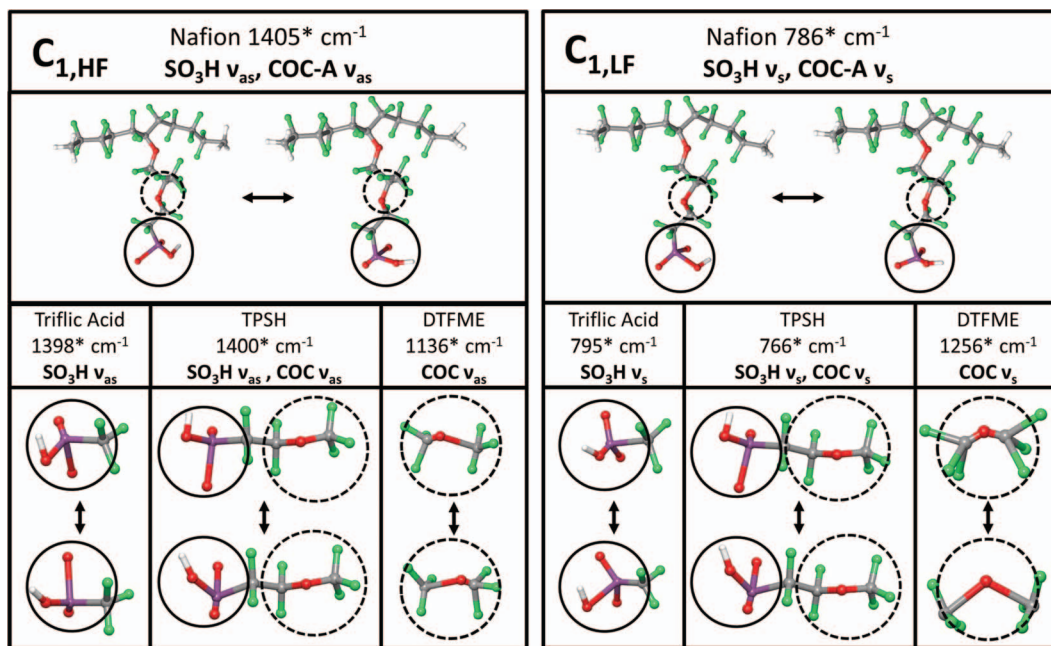


Figure 7. Extrema snapshots of normal mode eigenvector animations of dehydrated Nafion-[H], 2-trifluoromethoxy-perfluoroethane-2-sulfonic acid (TPSH), triflic acid, and di(trifluoromethyl)ether (DTFME). Dominant and secondary normal mode contributions identified by solid and dotted lines respectively.

C_{3V} normal mode eigenvector animation snapshots.—The fully hydrated Nafion spectrum (red) features bands at 1061 cm^{-1} and 969 cm^{-1} that correspond to the sulfonate form (C_{3V} local symmetry) of the exchange site. Eigenvector animation extrema screenshots (Fig. 8, top panels) provide details of the vibrational motions. These high ($C_{3V,HF}$) and low frequency ($C_{3V,LF}$) bands correspond to group modes that involve the same side-chain functional group contributors. Figure 8 depicts extrema of the C_{3V} normal mode eigenvector animations of hydrated Nafion and Nafion side chain composition analog structures. The lower panels show extrema snapshots of molecules that make up pure modes contributing to the C_{3V} group modes along with associated calculated normal mode frequencies. Both the $C_{3V,LF}$ and $C_{3V,HF}$ modes are group modes with participation of a dissociated sulfonate group with C_{3V} symmetry. The lower frequency 969 cm^{-1}

($C_{3V,LF}$) is dominated by a symmetric sulfonate stretch. (Fig. 8) The higher frequency 1061 cm^{-1} ($C_{3V,HF}$) has a major contribution from COC-A.

Historically, 969 cm^{-1} was ascribed solely to the COC ν_{as} , and the 1061 cm^{-1} was ascribed solely to the $\text{SO}_3^{-1}\nu_s$.⁵² In contrast, normal mode analyses of Nafion, DTFME, and triflate show why these bands cannot be properly assigned as single function group modes. The mirrored similarities of hydrated Nafion group modes, and its side chain pure modes, are evident in extrema snapshots (Fig. 8). As expected, our assignments are in line with the DTFME COC ν_{as} and triflate $\text{SO}_3^{-1}\nu_s$ modes at 1136 cm^{-1} and 981 cm^{-1} , respectively. Comparison of the pure modes (bottom panels) with the calculated normal modes (top panels) correctly show that the pure mode frequencies contributing to the $C_{3V,LF}$ are on average substantially higher than the

Table I. Group mode assignments, DFT calculated normal modes, Transmission IR, Raman bands for hydrated Nafion-[H], dehydrated Nafion-[H], TPS^- , TPSH, triflate, triflic acid and DTFME.

	Local symmetry	Group mode assignment	DFT (cm^{-1})	Transmission (cm^{-1})	Raman (cm^{-1})	Suppl. material
Hydrated Nafion-[H]		$\text{CF}_3\delta_u$, COC-B δ_s , COC-A δ_s	738*		730	Video S1
		BB	883*		806	Video S2
	$C_{3V,LF}$	$\text{SO}_3^{-1}\nu_s$, COC-A ν_{as}	983*	969	969	Video S3
	$C_{3V,HF}$	COC-A ν_{as} , $\text{SO}_3^{-1}\nu_s$	1059*	1061	1066	Video S4
Dehydrated Nafion-[H]		$\text{CF}_3\delta_u$, COC-B ρ_r , COC-A ρ_r	731*		730	Video S5
	$C_{1,LF}$	$\text{SO}_3\text{H}\nu_s$, COC-A ν_s	786*	910	910	Video S6
		COC(B) ω , BB	820*		806	Video S7
	$C_{1,HF}$	$\text{SO}_3\text{H}\nu_{as}$, COC-A ν_{as}	1405*	1414		Video S8
TPS^-	$C_{3V,LF}$	$\text{SO}_3^{-1}\nu_s$, COC ν_{as}	972*			Video S9
	$C_{3V,HF}$	COC ν_{as} , $\text{SO}_3^{-1}\nu_s$	1075*			Video S10
TPSH	$C_{1,LF}$	$\text{SO}_3\text{H}\nu_s$, COC ν_s	766*			Video S11
	$C_{1,HF}$	$\text{SO}_3\text{H}\nu_{as}$, COC ν_{as}	1400*			Video S12
Pure Modes						
Triflate	C_{3V}	$\text{SO}_3^{-1}\nu_s$	981*			Video S13
Triflic Acid	C_1	$\text{SO}_3\text{H}\nu_s$	795*			Video S14
	C_1	$\text{SO}_3\text{H}\nu_{as}$	1398*			Video S15
DTFME		COC ν_{as}	1136*			Video S16
		COC ν_s	1256*			Video S17

Symmetric stretching, ν_s ; Asymmetric stretching, ν_{as} ; Wagging, ω ; Bending, δ_s ; Umbrella bending, δ_u ; Rocking, ρ_r ; Backbone, BB; Calculated value*

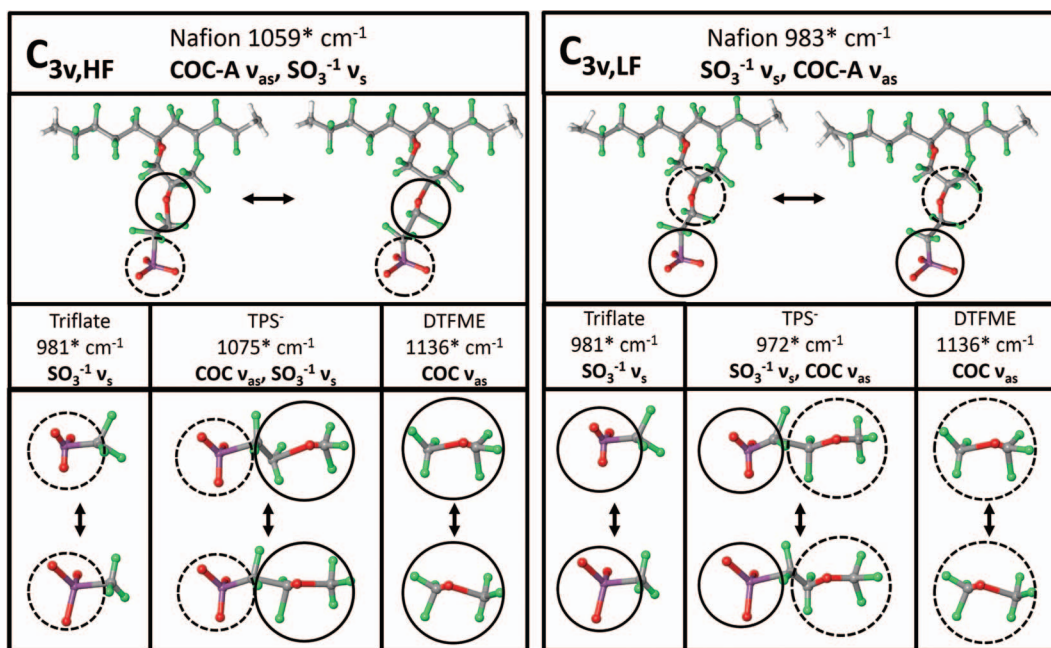


Figure 8. Extrema snapshots of normal mode eigenvector animations of hydrated Nafion-[H], 2-trifluoromethoxy-perfluoroethane-2-sulfonate (TPS-), triflate, and di(trifluoromethyl)ether (DTFME). Dominant and secondary normal mode contributions identified by solid and dotted lines respectively.

pure modes contributing to the $C_{3v,LF}$, in further support of the assignments. The relationships between pure modes and calculated normal modes (actually group modes) are more easily seen by visualization of the full animations, which are available as Supplemental Material. All of the assignments are summarized in Table I.

Intermediate states-of-hydration show coexistence of the C_{3v} and C_1 modes (Fig. 6 purple spectrum). Both C_{3v} and C_1 modes exist in the Raman spectra between 900 and 700 mV, consistent with the onset current (Fig. 5) and intermediate hydration. Thus C_1 and C_{3v} modes together are indicators of membrane state-of-hydration at intermediate and extreme levels. This is the most important revelation of Figure 6.

Nafion Raman bands at 730 cm^{-1} and 806 cm^{-1} .—Prior to this work, the bands at 730 cm^{-1} and 806 cm^{-1} had not been assigned by visualization of normal mode eigenvector animations. Although these Raman bands appear at all potentials (Fig. 6, left), there are band shape and intensity transitions concurrent with the onset of water formation (Fig. 6, dotted line region). Eigenvector animations (Figs. S1-2, 5, 7) reveal a pair of near degenerate normal modes that make up the 730 cm^{-1} band and another normal mode pair contributing to the 806 cm^{-1} band. While both observed bands are assigned by Peng et al.⁴⁹ as “due to Teflon skeleton structure”, the eigenvector animations enable a more detailed set of assignments.

The animations show that the 731* cm^{-1} (sulfonic acid side-chain normal mode analysis) and the 738* cm^{-1} (sulfonate side-chain normal mode analysis) both contribute to the 730 cm^{-1} band (Table I) to extents that depend on the state-of-hydration. Above 900 mV, the mode corresponding to the dehydrated exchange site dominates contributions (side-chain rocking) to the 730 cm^{-1} band. Between 900 and 700 mV, modes due to the dehydrated and hydrated states contribute to the band as the cathode initiates water formation. Below 700 mV, the modes associated with the dehydrated states are entirely supplanted by modes calculated from the hydrated state of the exchange site. The hydrated form of the exchange site becomes the dominant contributor (side-chain bending) to the 730 cm^{-1} band. Thus, there is a transition in the 730 cm^{-1} band as the membrane state of hydration increases. The band shape changes from a side-chain rocking dehydrated mode to a side-chain bending hydrated mode (low intensity, broad peaks to narrower, sharp peaks). The overall changes in modes are indirectly related to exchange site local symmetry because the animations show

little contribution of exchange site motions to the modes. However high and low states of hydration do have substantial impact on the overall morphology of the membrane (e.g., a three phase model,⁵⁶ core-shell structure,^{57,58} rod-like model,⁵⁹ etc.).

Similarly, normal mode animations confirm that the 820* cm^{-1} (sulfonic acid form) and 883* cm^{-1} (sulfonate form) normal modes contribute to the 806 cm^{-1} band (Table I). Above 900 mV, the 820* cm^{-1} mode dominates contributions (side-chain/backbone) to the 806 cm^{-1} band. Between 900 and 700 mV, the 820* cm^{-1} and 883* cm^{-1} modes co-contribute to the 806 cm^{-1} band as the cathode initiates water formation. Below 700 mV, the 820* cm^{-1} mode is entirely supplanted by the 883* cm^{-1} mode. In summary, as the membrane becomes hydrated, the dominant contributor to the 806 cm^{-1} band gradually shifts from the calculated 820* cm^{-1} to the 883* cm^{-1} normal modes. The band shape changes (although not as distinctly as in the 730 cm^{-1} band) from a side-chain/backbone dehydrated mode to a backbone hydrated mode.

Raman bands (560 – 631 cm^{-1}).—Figure 6 shows low intensity bands at 564 cm^{-1} , 600 cm^{-1} , and 635 cm^{-1} . To facilitate analysis, Figure 9 shows operando spectra with cathode catalytic layers of: (left) Fe-N_x/C (O₂ flow), (middle) C/(no Fe-N_x/C) (O₂ flow), and (right) Fe-N_x/C (N₂ flow). Johnson Matthey Pt/C was used at the MEA anode. The absence of peak frequency potential dependence (Stark tuning) justifies signal averaging of the left, middle and right panel spectra. “Average” spectra are shown in separate panels below their respective source panels.

The peak at 564 cm^{-1} , attributed to Fe-O₂ stretching modes,^{60–63} is present at all cell potentials under O₂ flow (left). It is non-discernable from the background under N₂ flow (right). There is total absence of intensity at 564 cm^{-1} when a carbon cathode is under O₂ flow (middle). This is totally consistent with the presence of iron in the catalytic layer. However, the absence of Stark tuning of the Fe-O₂ stretching modes, and the appearance of the peak at potentials from open circuit to short circuit currents is unexpected for a site associated with the oxygen reduction current onset.

A literature search revealed no reports of Fe-O₂ stretching modes within the 600 cm^{-1} to 635 cm^{-1} range. However, a Hester and Krishnan⁶⁴ report on vibrational spectra of divalent metals in molten sulfates elucidates an analogy between metal complexation in molten

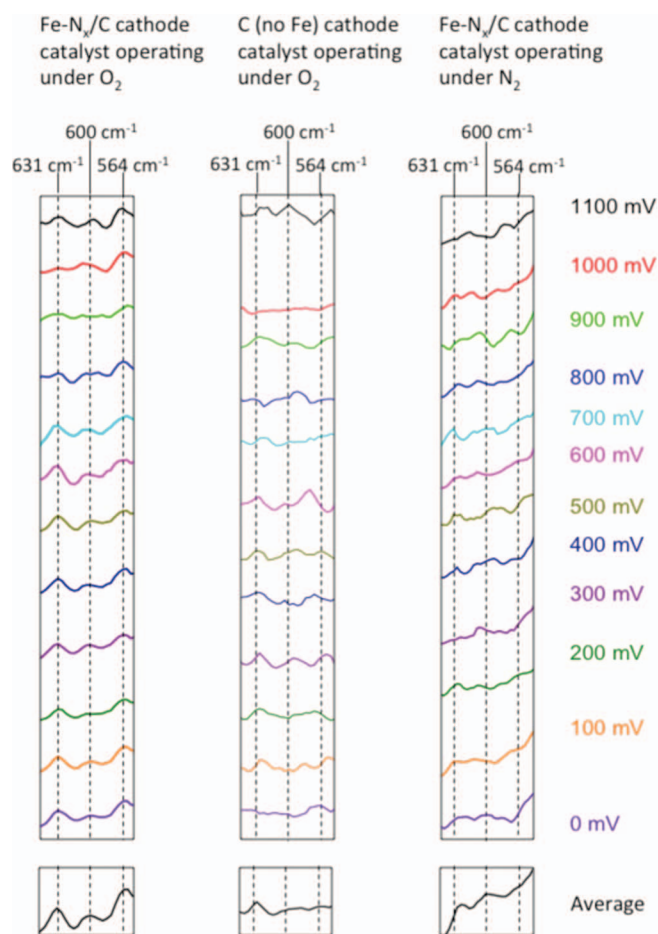


Figure 9. Potential dependent Raman spectra, from 650 to 550 cm^{-1} , of the Fe-N_x/C cathode catalyst operating under O₂ (left), C (no Fe) cathode catalyst operating under O₂ (middle), and Fe-N_x/C cathode catalyst operating under N₂ (right).

sulfates and that of divalent ions with the exchange site of dehydrated Nafion. We reported that divalent ions in dehydrated Nafion bind with C_{3v} symmetry^{48–50} to sulfonate oxygens. Hester and Krishnan confirmed C_{3v} binding of divalent metals to dry molten sulfonates. Buzgar et al.⁶⁵ further support C_{3v} binding of transition metals to sulfonates in the wavenumber region 600 cm^{-1} to 635 cm^{-1} . The above references, a report by Brogan et al.⁶⁶ on Pt-O vibrational modes and the high performance of fuel cell of this study suggests that other metal oxygen interactions may be contributing to vibrational spectral features in Figures 6 and 9. We recently reported on the direct interaction of Pt with the Nafion sulfonate group²² and the emergence of Nafion bands at similar operando spectroscopy fuel cell potentials in Pt cathode fuel cells.¹⁸ The possibility of a Pt contaminant in the as-received Fe-N_x/C catalyst prompted us to request a Pt analysis by Robertson Microlit Laboratories, Ledgewood, NJ. The analysis showed 13.4 ppm Pt in the as-received catalyst.^d

This section points out the need for high resolution operando spectroscopy of Pt and non-PGM catalysts within the 550 – 650 cm^{-1} region. Previous reports on molten sulfate Raman spectroscopy that complement our findings that Nafion side-chain group modes are best categorized in terms of local symmetry⁵⁰ provide impetus for these further studies.

^dThe original vial with remaining catalyst was sent for ICP-MS analysis.

Conclusions

Hydrogen/oxygen fuel cell operando Raman spectroscopy shows the potential-dependent spectroscopy of the Nafion ionomer within the MEA cathode catalytic layer: The ionomer state-of-hydration increases as the fuel cell voltage decreases. Density functional theory calculated normal mode analysis, of the Nafion repeat unit and side-chain molecular fragment analogs, provides eigenvector animations that enable Nafion band assignments in terms of the exchange site local symmetry. Dehydrated Nafion features C₁ modes that are associated with the sulfonic acid form of the exchange site. Hydrated Nafion features C_{3v} modes that are associated with the sulfonate form. At intermediate stages of hydration the C₁ and C_{3v} modes coexist. The study highlights a less understood wavenumber region between 550 and 650 cm^{-1} .

The proper positioning of the Raman microscope laser focal point is determined by a coarse depth profiling of the Raman fuel cell that is calibrated by Raman peaks associated with materials that comprise layered regions of the fuel cell device. This technique can advance the fundamental understanding of the processes such as oxygen reduction reaction (ORR), carbon corrosion, and catalysis process of ORR in PEMFCs catalyzed by Pt or non-PGM catalysts operating under realistic conditions.

Acknowledgments

Thanks are due to Prof. Scott Calabrese Barton from Michigan State University for providing the catalysts and both the US Department of Energy EERE (DE-EE-0000459), and the Army Research Office for funding (W911NF-12-1-0346).

References

- H. Topsoe, "Developments in operando studies and in situ characterization of heterogeneous catalysts," *Journal of Catalysis*, **216**(1-2), 155 (2003).
- B. M. Weckhuysen, "Snapshots of a working catalyst: possibilities and limitations of in situ spectroscopy in the field of heterogeneous catalysis," *Chemical Communications*, **97** (2002).
- M. S. Wilson and S. Gottesfeld, "Thin-Film Catalyst Layers for Polymer Electrolyte Fuel-Cell Electrodes," *J. Appl. Electrochem.*, **22**, 1 (1992).
- S. Gottesfeld et al., *Advances in Direct Methanol Fuel Cell Science & Technology at Los Alamos National Laboratory*, 2000, Los Alamos National Laboratory: Los Alamos, New Mexico 87545, USA.
- R. Liu et al., "A coulometric normalization procedure for comparing high surface area methanol anode catalysts by rotating disk electrode voltammetry," *Journal of the Electrochemical Society*, **144**(6), L148 (1997).
- R. Liu et al., "A coulometric normalization procedure for comparing high surface area methanol anode catalysts by rotating disk electrode voltammetry (vol 144, pg L148, 1997)," *Journal of The Electrochemical Society*, **144**(8), 2942 (1997).
- Q. B. Fan, C. Pu, and E. S. Smotkin, "In situ Fourier transform infrared-diffuse reflection spectroscopy of direct methanol fuel cell anodes and cathodes," *Journal Of The Electrochemical Society*, **143**(10), 3053 (1996).
- R. Viswanathan et al., "In-Situ XANES of Carbon-Supported Pt-Ru Anode Electrocatalyst for Reformate-Air Polymer Electrolyte Fuel Cells," *Journal of Physical Chemistry B*, **106**(13), 3458 (2002).
- R. Viswanathan, R. Liu, and E. S. Smotkin, "In situ X-ray absorption fuel cell," *Review of Scientific Instruments*, **73**(5), 2124 (2002).
- S. Stoupin et al., "Pt and Ru X-ray Absorption Spectroscopy of PtRu Anode Catalysts in Operating Direct Methanol Fuel Cells," *Journal of Physical Chemistry B*, **110**(20), 9932 (2006).
- E. Principi et al., "An XAS experimental approach to study low Pt content electrocatalysts operating in PEM fuel cells," *Phys Chem Chem Phys*, **11**(43), 9987 (2009).
- R. J. K. Wiltshire et al., "A PEM fuel cell for in situ XAS studies," *Electrochimica Acta*, **50**(25-26), 5208 (2005).
- N. Ishiguro et al., "Operando Time-Resolved X-ray Absorption Fine Structure Study for Surface Events on a Pt3Co/C Cathode Catalyst in a Polymer Electrolyte Fuel Cell during Voltage-Operating Processes," *ACS Catalysis*, **2**(7), 1319 (2012).
- M. Watanabe et al., "Overview of recent developments in oxygen reduction electrocatalysis," *Electrochimica Acta*, **84**, 187 (2012).
- D. E. Ramaker et al., "Following ORR intermediates adsorbed on a Pt cathode catalyst during break-in of a PEM fuel cell by in operando X-ray absorption spectroscopy," *Physical Chemistry Chemical Physics*, **16**(27), 13645 (2014).
- T. Sakamoto et al., "Operando XAFS study of carbon supported Ni, NiZn, and Co catalysts for hydrazine electrooxidation for use in anion exchange membrane fuel cells," *Electrochimica Acta*, **163**, 116 (2015).
- J. A. Gilbert et al., "Pt Catalyst Degradation in Aqueous and Fuel Cell Environments studied via In-Operando Anomalous Small-Angle X-ray Scattering," *Electrochimica Acta*, **173**, 223 (2015).

18. I. Kendrick and E. S. Smotkin, "Operando infrared spectroscopy of the fuel cell membrane electrode assembly Nafion-platinum interface," *International Journal of Hydrogen Energy*, **39**(6), 2751 (2014).
19. I. Kendrick, J. Doan, and E. S. Smotkin, *Vibrational Spectroscopy of the Ionomer-Catalyst Interface*. "Vibrational Spectroscopy at Electrified Interfaces," ed. A. Wieckowski, C. Korzeniewski, and B. Braunschweig. 2013, Oxford: Blackwell Science Publ. 327.
20. S. E. Everts et al., "Ensemble Site Requirements for Oxidative Adsorption of Methanol and Ethanol on Pt Membrane Electrode Assemblies," *ACS Catalysis*, **2**(5), 701 (2012).
21. E. A. Lewis et al., "Operando X-ray absorption and infrared fuel cell spectroscopy," *Electrochimica Acta*, **56**(24), 8827 (2011).
22. I. Kendrick et al., "Elucidating the Ionomer-Electrified Metal Interface," *Journal of the American Chemical Society*, **132**(49), 17611 (2010).
23. E. S. Smotkin, *FTIR and X-ray Absorption Spectroscopy of Operating Fuel Cells*, in "In situ Spectroscopic Studies of Adsorption at the Electrode and Electrocatalysis," S. Shi-Gang, C. Paul Andrew, and W. Andrzej, Editors. 2007, Elsevier Science B. V.: Amsterdam, p. 247.
24. S. Sanicharane et al., "In situ 50 DegC FTIR spectroscopy of Pt and PtRu direct methanol fuel cell membrane electrode assembly anodes," *Journal of the Electrochemical Society*, **149**(5), A554 (2002).
25. A. L. Bo et al., "In situ Stark effects with inverted bipolar peaks for adsorbed CO on Pt electrodes in 50 degrees C direct methanol fuel cells," *Journal Of Physical Chemistry B*, **104**(31), 7377 (2000).
26. K. L. Ley et al., "Methanol oxidation on single-phase Pt-Ru-Os ternary alloys," *Journal of the Electrochemical Society*, **144**(5), 1543 (1997).
27. Q. B. Fan et al., "In situ FTIR-diffuse reflection spectroscopy of the anode surface in a direct methanol/oxygen fuel cell," *Journal of The Electrochemical Society*, **143**(2), L21 (1996).
28. R. C. Maher and L. F. Cohen, "Raman spectroscopy as a probe of temperature and oxidation state for gadolinium-doped ceria used in solid oxide fuel cells," *Journal of Physical Chemistry A*, **112**(7), 1497 (2008).
29. M. B. Pomfret, J. C. Owrutsky, and R. A. Walker, "In situ studies of fuel oxidation in solid oxide fuel cells," *Analytical Chemistry*, **79**(6), 2367 (2007).
30. H. W. Abernathy et al., "Monitoring Ag-Cr interactions in SOFC cathodes using Raman spectroscopy," *Journal of Physical Chemistry C*, **112**(34), 13299 (2008).
31. Z. Peng et al., "Depth-resolved micro-Raman spectroscopy of tri-layer PFSA membrane for PEM fuel cells: how to obtain reliable inner water contents," *Journal of Raman Spectroscopy*, **44**(2), 321 (2013).
32. P. Huguet et al., "In situ analysis of water management in operating fuel cells by confocal Raman spectroscopy," *Electrochemistry Communications*, **13**(5), 418 (2011).
33. Y. Tabuchi et al., "Analysis of in situ water transport in Nafion (R) by confocal micro-Raman spectroscopy," *Journal of Power Sources*, **196**(2), 652 (2011).
34. M. Hara et al., "Temperature dependence of the water distribution inside a Nafion membrane in an operating polymer electrolyte fuel cell. A micro-Raman study," *Electrochimica Acta*, **58**, 449 (2011).
35. H. Matic et al., "In situ micro-Raman on the membrane in a working PEM cell," *Electrochemical and Solid State Letters*, **8**(1), A5 (2005).
36. W. A. Rigdon and X. Y. Huang, "Carbon monoxide tolerant platinum electrocatalysts on niobium doped titania and carbon nanotube composite supports," *Journal of Power Sources*, **272**, 845 (2014).
37. P. Hohenberg and W. Kohn, "Inhomogeneous Electron Gas," *Physical Review*, **136**(3B), B864 (1964).
38. X. Xu et al., "An extended hybrid density functional (X3LYP) with improved descriptions of nonbond interactions and thermodynamic properties of molecular systems," *Journal of Chemical Physics*, **122**(1), 14 (2005).
39. A. D. Becke, "Density-Functional Thermochemistry 3. The Role of Exact Exchange," *Journal of Chemical Physics*, **98**(7), 5648 (1993).
40. W. Kohn and L. J. Sham, "Self-Consistent Equations Including Exchange and Correlation Effects," *Physical Review*, **140**(4A), A1133 (1965).
41. V. Nallathambi et al., "Nitrogen Precursor Effects in Iron-Nitrogen-Carbon Oxygen Reduction Catalysts," *Electrochemical and Solid State Letters*, **14**(6), B55 (2011).
42. B. Gurau and E. S. Smotkin, "Methanol crossover in direct methanol fuel cells: a link between power and energy density," *J. Power Sources*, **112**, 339 (2002).
43. D. Bomse and M. N. Ediger, "Simultaneous Detection of Multiple Gases by Raman Spectroscopy with Hollow-Core Fibers," in *CLEO: Science and Innovations*. 2014, Optical Society of America.
44. I. Kendrick, J. Doan, and E. S. Smotkin, "Vibrational Spectroscopy of the Ionomer-Catalyst Interface, in *Vibrational Spectroscopy at Electrified Interfaces*, A. Wieckowski, C. Korzeniewski, and B. Braunschweig, Editors. 2013, p. 327.
45. Q. J. Duan, H. P. Wang, and J. Benziger, "Transport of liquid water through Nafion membranes," *Journal of Membrane Science*, **392**, 88 (2012).
46. F. Jaouen, F. Charretre, and J. P. Dodelet, "Fe-based catalysts for oxygen reduction in PEMFCs - Importance of the disordered phase of the carbon support," *Journal of the Electrochemical Society*, **153**(4), A689 (2006).
47. I. Kendrick et al., "Operando Raman and Theoretical Vibration Spectroscopy of Non-PGM Catalysts, 2012, *Presentation about spectroscopy techniques for non-platinum group metal (PGM) catalysts at the kick-off meeting of the U.S. Department of Energy Fuel Cell Technologies Program's Catalysis Working Group*. http://energy.gov/sites/prod/files/2014/03/f10/6_cwg_may2012_smotkin.pdf.
48. I. Kendrick et al., "Theoretical and Experimental Infrared Spectra of Hydrated and Dehydrated Nafion," *Journal of Polymer Science Part B-Polymer Physics*, **51**(18), 1329 (2013).
49. M. Webber et al., "Mechanically Coupled Internal Coordinates of Ionomer Vibrational Modes," *Macromolecules*, **43**(13), 5500 (2010).
50. J. Doan et al., "Symmetry-based IR group modes as dynamic probes of Nafion ion exchange site structure," *Polymer*, **73**, 34 (2015).
51. J. Doan et al., "Theoretical and experimental infrared spectra of hydrated and dehydrated sulfonated poly(ether ether ketone)," *Polymer*, **55**(18), 4671 (2014).
52. K. M. Cable, K. A. Mauritz, and R. B. Moore, "Effects of hydrophilic and hydrophobic counterions on the Coulombic interactions in perfluorosulfonate ionomers," *Journal of Polymer Science, Part B: Polymer Physics*, **33**(7), 1065 (1995).
53. D. S. Warren and A. J. McQuillan, "Infrared spectroscopic and DFT vibrational mode study of perfluoro(2-ethoxyethane) sulfonic acid (PES), a model Nafion side-chain molecule," *Journal of Physical Chemistry B*, **112**(34), 10535 (2008).
54. C. K. Byun et al., "Infrared Spectroscopy of Bis (perfluoroalkyl)sulfonyl Imide Ionomer Membrane Materials," *Journal of Physical Chemistry B*, **113**(18), 6299 (2009).
55. Y. Okamoto, "An ab initio study of the side chain of Nafion," *Chemical Physics Letters*, **389**(1-3), 64 (2004).
56. H. L. Yeager and A. Steck, "Cation and Water Diffusion in Nafion Ion Exchange Membranes: Influence of Polymer Structure," *Journal Of The Electrochemical Society*, **128**(9), 1880 (1981).
57. M. Fujimura, T. Hashimoto, and H. Kawai, "Small-Angle X-ray Scattering Study of Perfluorinated Ionomer Membranes. 1. Origin of Two Scattering Maxima," *Macromolecules*, **14**, 1309 (1981).
58. G. Gebel et al., "The kinetics of water sorption in Nafion membranes: a small-angle neutron scattering study," *Journal of Physics-Condensed Matter*, **23**(23), (2011).
59. L. Rubatat et al., "Evidence of Elongated Polymeric Aggregates in Nafion," *Macromolecules*, **35**, 4050 (2002).
60. T. K. Das et al., "Simultaneous observation of the O-O and Fe-O-2 stretching modes in oxyhemoglobins," *Proceedings of the National Academy of Sciences of the United States of America*, **98**(2), 479 (2001).
61. R. Holze, "Electrochemical and Surface Raman-Spectroscopic Studies of an Iron Porphyrin Adsorbed on an Electrode," *Electrochimica Acta*, **33**(11), 1619 (1988).
62. J. M. Burke, J. R. Kincaid, and T. G. Spiro, "Resonance Raman-Spectra and Vibrational Modes of Iron(II) Tetraphenylporphyrin Mu-Oxo Dimer - Evidence for Phenyl Interaction and Lack of Dimer Splitting," *Journal of the American Chemical Society*, **100**(19), 6077 (1978).
63. J. M. Burke et al., "Structure-Sensitive Resonance Raman Bands of Tetraphenyl and Picket Fence Porphyrin-Iron Complexes, Including an Oxyhemoglobin Analog," *Journal of the American Chemical Society*, **100**(19), 6083 (1978).
64. R. Hester and K. Krishnan, "Vibrational Spectra of Molten Salts. V. Infrared and Raman Spectra of Some Molten Sulfates," *The Journal of Chemical Physics*, **49**(10), 4356 (1968).
65. N. Buzgar, A. Buzatu, and I. V. Sanislav, "The Raman study on certain sulfates," *An. Stiint. U. Al. I-Mat*, **55**(1), 5 (2009).
66. M. S. Brogan, T. J. Dines, and J. A. Cairns, "Raman spectroscopic study of the Pt-CeO2 interaction in the Pt/Al2O3-CeO2 catalyst," *Journal of the Chemical Society, Faraday Transactions*, **90**(10), 1461 (1994).